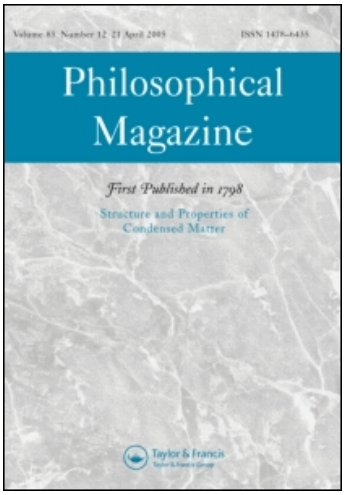

Philosophical Magazine
Publication details, including instructions for authors and subscription information:
http://www.informaworld.com/smpp/title~content=t713695589

Morphology and orientation of iron oxide precipitates in epitaxial $BiFeO_3$ thin films grown under two non-optimized oxygen pressures

X. Wang[a]; Y. L. Zhu[a]; S. B. Mi[a]; C. Wang[b]; H. B. Lu[b]; X. L. Ma[a]
[a] Shenyang National Laboratory for Materials Science, Institute of Metal Research, Chinese Academy of Sciences, Shenyang 110016, China [b] Beijing National Laboratory for Condensed Matter Physics, Institute of Physics, Chinese Academy of Sciences, Beijing 100190, China

First published on: 20 September 2010

To cite this Article Wang, X. , Zhu, Y. L. , Mi, S. B. , Wang, C. , Lu, H. B. and Ma, X. L.(2010) 'Morphology and orientation of iron oxide precipitates in epitaxial $BiFeO_3$ thin films grown under two non-optimized oxygen pressures', Philosophical Magazine, 90: 34, 4551 — 4567, First published on: 20 September 2010 (iFirst)
To link to this Article: DOI: 10.1080/14786435.2010.515261
URL: http://dx.doi.org/10.1080/14786435.2010.515261

Philosophical Magazine
Vol. 90, No. 34, 28 November 2010, 4551–4567

Taylor & Francis
Taylor & Francis Group

Morphology and orientation of iron oxide precipitates in epitaxial $BiFeO_3$ thin films grown under two non-optimized oxygen pressures

X. Wang[a], Y.L. Zhu[a]*, S.B. Mi[a], C. Wang[b], H.B. Lu[b] and X.L. Ma[a]

[a]*Shenyang National Laboratory for Materials Science, Institute of Metal Research, Chinese Academy of Sciences, Shenyang 110016, China;* [b]*Beijing National Laboratory for Condensed Matter Physics, Institute of Physics, Chinese Academy of Sciences, Beijing 100190, China*

(*Received 1 June 2010; final version received 9 August 2010*)

Microstructures of multiferroic $BiFeO_3$ thin films epitaxially grown on $SrRuO_3$-buffered $SrTiO_3$ (001) substrates by laser molecular-beam epitaxy under two non-optimized oxygen pressures were characterized by means of transmission electron microscopy. The results showed that the films grown under oxygen pressures of 1 Pa and 0.3 Pa contain a secondary phase embedded in the $BiFeO_3$ matrix. High-angle annular dark-field imaging, elemental mapping and composition analysis in combination with selected area electron diffraction revealed that the parasitic phase is mainly antiferromagnetic α-Fe_2O_3. The α-Fe_2O_3 particles are semi-coherently embedded in the $BiFeO_3$ films, as confirmed by high-resolution transmission electron microscopy. In addition to the α-Fe_2O_3 phase, ferromagnetic Fe_3O_4 precipitates were found in the $BiFeO_3$ films grown under 0.3 Pa and shown to accumulate in areas near the film/substrate interfaces. In our heteroepitaxy systems, very low density misfit dislocations were observed at the interfaces between the $BiFeO_3$ and $SrRuO_3$ layers implying that their misfit strains may be relieved by the formation of the secondary phases. Using X-ray photoelectron spectroscopy it was found that Fe exists in the +3 oxidation state in these films. The possible formation mechanisms of the secondary phases are discussed in terms of film growth conditions.

Keywords: transmission electron microscopy; bismuth ferrite; multiferroic film; secondary phase; microstructure

1. Introduction

In the past few years, magnetoelectric multiferroic materials have attracted considerable attention not only from the aspect of fundamental physics but also due to their potential applications in novel technological devices [1,2]. There are very few single-phase multiferroic materials due to chemical incompatibility of both ferromagnetism and ferroelectricity [3]. Among them, $BiFeO_3$ (BFO) is perhaps the only one with both (anti-) ferromagnetic and ferroelectric ordering coexisting at room temperature [4]. BFO is antiferromagnetic with the weak local canting moment being completely cancelled by the averaging out effect of the cycloid. Recently the

*Corresponding author. Email: ylzhu@imr.ac.cn

ISSN 1478–6435 print/ISSN 1478–6443 online

DOI: 10.1080/14786435.2010.515261
http://www.informaworld.com

large remnant polarization has been shown in both high quality BFO thin films [5] and single crystals [6]. Furthermore, it has been proved that the magnetic easy planes rotate when the polarization changes direction in BFO thin films [7] and single crystals [8], which makes voltage control of magnetization possible.

One of the most important difficulties that impede BFO films for practical applications is its compositional instability, which is believed to be the reason for its fickleness of functional behavior. Pure BFO films can only be obtained in a narrow deposition pressure and temperature window [9]. Outside of optimized conditions, parasitic phases such as Bi_2O_3 and Fe oxides form; however, it is difficult to detect these impurity concentrations by standard X-ray diffraction measurements, which is likely due to the epitaxial formation of them in BFO films. It was shown that by varying deposition oxygen pressure, the main phase formed in the BFO films grown by pulsed laser deposition changes from single phase of BFO to a mixture of BFO, α-Fe_2O_3 and γ-Fe_2O_3, as detected by X-ray absorption spectroscopy, X-ray magnetic circular dichroism and advanced X-ray diffraction measurements [10], or α-Fe_2O_3+BFO, as observed by means of transmission electron microscopy (TEM) [11].

On the one hand, the formation of these parasitic phases may influence the measured properties of the Bi–Fe–O films. For example, it was confirmed that BFO films have low intrinsic magnetic moment [12], and the origin of ferromagnetic signal in BFO films in earlier paper [5] was suggested to be the ferromagnetic γ-Fe_2O_3 precipitates [10,13], the presence of Fe^{2+} in the films [14,15], or the formation of Fe_3O_4 under dc voltage stressing [16]. Previously, it was reported that the polarization of pure BFO was intrinsically high and relatively insensitive to epitaxial strain [17,18]. The low values of the polarization may result from chemical fluctuation. A small amount of impure phase α-Fe_2O_3 slightly lowered the polarization value through pinning of the domain switching [19]. The existence of Fe^{2+} and oxygen vacancies increased the leakage current and depressed the ferroelectric properties [15,20,21]. Even for high quality BFO films, the dominated leakage mechanism of BFO with symmetric SRO electrodes was demonstrated to be Poole–Frenkel emission, and the measured trap ionization energy corresponded to the ionization of Fe^{2+} ions [22]. The observed chemical fluctuations may root in chemical point defects in the pure BFO phase or the nano-sized impure phase; nevertheless, the origin of it remained unclear, and little probe was performed on local chemical compositions and structures in BFO films.

On the other hand, composite metal oxides with two functional constituents can lead to additional functions [2]. Nanocomposite films with a vertical architecture could offer a larger interfacial strain and enhance the interfacial interaction [23]. Self-assembled nanocomposite films with an ordered nanocolumnar structure have been realized and the interfacial effects were investigated in $BiFeO_3$–$CoFe_2O_4$ [24] and $BiFeO_3$–Sm_2O_3 systems [25,26]. In Bi–Fe–O films systems, it was found that the BFO phase and several functional types of Fe oxides coexisted, and both highly strained and relaxed BFO regions were present in the same films [27]. The leakage current was reduced in these composite films compared to that of the pure BFO phase [11,26]. In order to pursue nanocomposite films of BFO coupled with functional Fe oxides, efforts are needed to clarify the association of the deposition conditions with the microstructures in the Bi–Fe–O compounds.

In this paper, a detailed study is presented of the microstructural characteristics in BFO films prepared at different oxygen pressures by laser molecular-beam epitaxy. Some α-Fe_2O_3 particles were found embedded in two as-received BFO films grown under oxygen pressures of 1 Pa and 0.3 Pa. Furthermore, in addition to α-Fe_2O_3 particles in the BFO film matrix, nano-sized precipitates of Fe_3O_4 were also observed in 0.3 Pa BFO films. The orientation relationships between these parasitic phases and the BFO film matrix were determined. In particular, our efforts focus on the study of the effects of these parasitic phases on misfit strain relaxation in BFO thin films. It is concluded that the misfit strains between the BFO films and the substrates are mainly relaxed by the formation of secondary phases. It is pointed out that by varying the ratio of BFO and α-Fe_2O_3 phases through adjusting oxygen pressure, multiferroic nanocomposite films could be obtained.

2. Experimental

Single crystal $SrTiO_3$ (STO) substrates were used to grow the films epitaxially. BFO films were prepared by laser molecular-beam epitaxy, employing a XeCl exciter laser with a wavelength of 308 nm. Ceramic targets of $SrRuO_3$ (SRO) and of $Bi_{1.05}FeO_3$ were used for *in situ* thin film deposition. The content of Bi was 5% excess in order to compensate for the high volatility of Bi and prevent Bi deficiency inside the films. The SRO layer was chosen as the bottom electrode. The BFO films were deposited at a substrate temperature of 550°C in a background atmosphere of 1 Pa or 0.3 Pa oxygen, with a laser energy density of 1.5 J cm^{-2}, at a laser repetition rate of 5 Hz.

TEM specimens for both cross-sectional and plan view observations were prepared by conventional methods, i.e. by slicing, grinding, dimpling, and finally ion-milling. Plan view specimens were ion-milled only from the substrate side. A Tecnai G^2 F30 transmission electron microscope, equipped with a high angle annular dark field (HAADF) detector and energy dispersive X-ray spectroscopy (EDS), was used at 300 kV for contrast analysis, lattice imaging, Z contrast imaging and composition line-scanning.

The surface and in-depth chemical composition was studied by means of X-ray photoelectron spectroscopy (XPS). XPS experiments were performed in a ESCALAB250 Multitechnique system with a monochromatic X-ray source (Al K_α line at 1486.6 eV and 150 W). The source was operated at an emission current of 10 mA and an anode voltage of 15 kV. The resolution for the spectra was 50.0 eV of pass energy and 0.05 eV/step. To correct the shifts in binding energies of core levels due to charging effect, the C 1*s* peak at 284.7 eV was used as an internal reference. Ion bombardment of sample surface was carried out with an argon ion gun. With this gun, it is possible to raster the ion beam evenly over an area 2 mm × 2 mm. Argon ions of 2 kV were used with a flux density of 2 μA. The beam intersected the surface at a glancing angle of 45°.

3. Results and discussion

3.1. *Parasitic phase in BFO film grown under oxygen pressure of 1 Pa*

Figure 1a shows a TEM bright field image of BFO films on SRO/STO substrates grown under an oxygen pressure of 1 Pa. It can be seen that a 630 nm thick BFO film

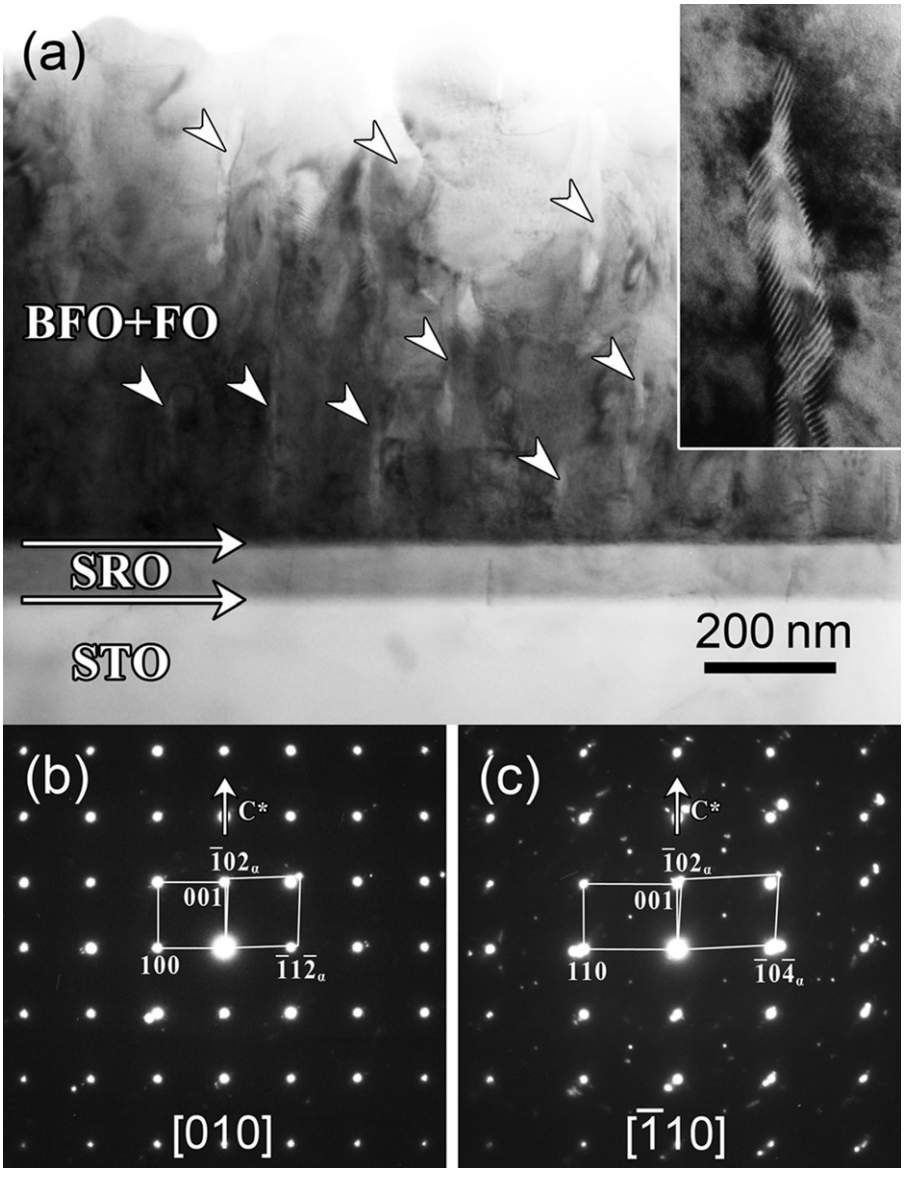

Figure 1. (a) Low-magnification cross-sectional bright-field image showing the morphology of BFO thin film grown on SRO-buffered STO (001) substrates at an oxygen pressure of 1 Pa. Some white particles can be observed in the film, as pointed out by arrowheads. The inset is an enlarged image showing the detail of one particle. Selected area electron diffraction patterns using an aperture covering both the BFO phase and the white particles: (b) [010] zone axis; and (c) [$\bar{1}$10] zone axis of BFO. BFO is treated as pseudocubic and the cell for BFO is outlined on the left. Extra spots can be observed, as denoted by the right grids and indexed as α-Fe_2O_3. Subscript α denotes α-Fe_2O_3 phase.

and a 100 nm thick SRO buffer layer are evident. The interfaces between the film and the substrates are sharp and flat, as denoted by white arrows. It is also found that some white particles are embedded in the film, as pointed out by arrowheads. To better see the morphology, an enlarged image is shown in the inset. The particle shows moiré fringe contrast. The sizes of these particles range from 20–50 nm wide and 20–200 nm long. Selected-area electron diffraction patterns (EDPs) covering the area including both the white particles and BFO matrix were obtained with the electron beam parallel to the [010] and [$\bar{1}$10] directions of pseudo-cubic BFO, respectively, as shown in Figures 1b and 1c. It is well known that bulk BFO is rhombohedral with the lattice parameters of $a_{rh} = 5.6343$ Å, $\alpha_{rh} = 59.348^\circ$ and space group symmetry of *R3c* [28]. In this paper, for the sake of convenience, BFO is indexed according to pseudo-cubic unit cell with $a_p = 3.962$ Å. Besides strong spots from BFO, as outlined with a square or a rectangle in Figures 1b and 1c, extra spots can be identified and they form a parallelogram, as denoted in the pattern, implying that parasitic phase may exist in the film. EDPs from other particles were also recorded and they are either the same as in Figures 1b and 1c or in mirror symmetry with it. This indicates that all particles of parasitic phase in this film have the same crystal structure and show definite orientation relationships with the BFO film. In Figure 1b, some extra weak spots from the parasitic phase are deviated by a few degrees along [101] direction of BFO to the exact zone axis due to rhombohedral symmetry; however, all the extra spots from the parasitic phase are on zone axis exactly in Figure 1c. This difference facilitates the determination of the orientation relationships between the parasitic phases and the BFO film matrix as discussed in the following.

A HAADF image of the same region as in Figure 1a is shown in Figure 2a, which provides composition information about the film. It can be seen that the white particles exhibit dark band contrast, indicating that heavier elements are poor in these bands compared with the bright contrast in adjacent areas. A detailed analysis on composition distribution was carried out by means of EDS line-scanning along the route marked by a white line in Figure 2a. The plots of composition fluctuation are given in Figure 2b. When the line-scan goes across the dark band contrast area, the count of Bi evidently decreases, whereas that of Fe increases rapidly, indicating that the particles are poor in Bi and rich in Fe. The spectra of the BFO film matrix and the parasitic phase were quantified and the atomic percentages are shown in Table 1. The particles contain much less Bi (2%) than the BFO matrix (24%), implying that the parasitic phase may be a type of iron oxide.

TEM investigation of a plan-view specimen provided structural information about the films from another direction. Figure 3a shows a low-magnification, plan-view BF image showing the distribution of the parasitic phase in the BFO film grown at 1 Pa. Moiré fringes can be seen at some particles of the parasitic phase at certain two beam conditions, which indicates that the particles are embedded in BFO film and that the set of its lattice and the set of BFO lattice have nearly common periodicities. Figure 3b shows the HAADF image of the same area as in Figure 3a. In accordance with the cross-sectional results above, the dark contrast of the particles indicates that heavy elements in the parasitic phase are less than in the BFO matrix. The selected-area EDP covering a relatively large area containing several precipitates of the parasitic phase and BFO matrix is shown in Figure 3c. This image was taken

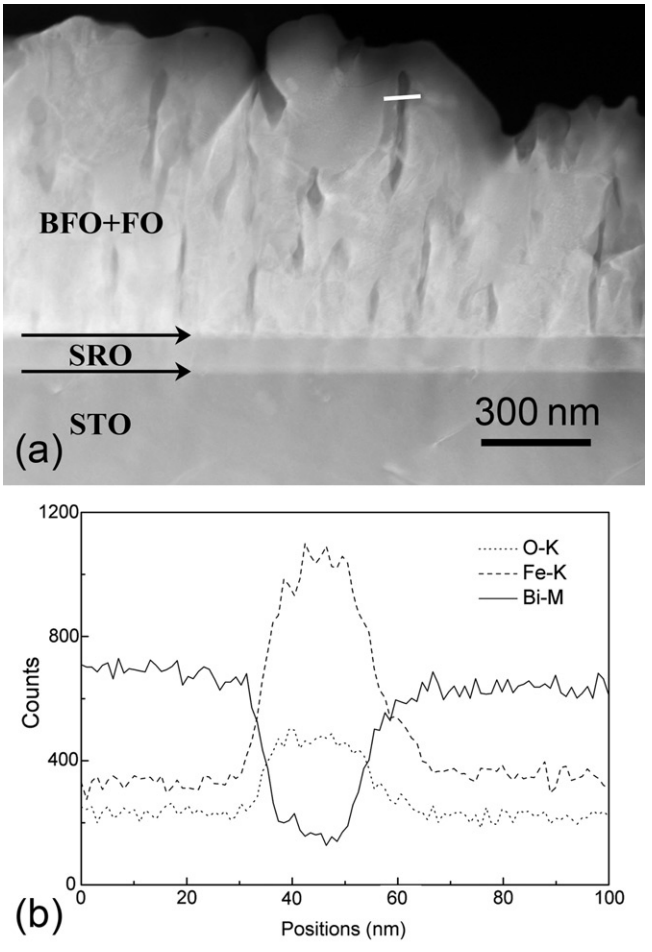

Figure 2. (a) HAADF image obtained from the same area as in Figure 1a. The dark contrast implies heavier elements are poor within the particles. (b) EDS plots showing composition fluctuation. The scanned route is marked with a white line in (a).

Table 1. Atomic percentages of Bi, Fe, and O calculated from the EDS spectrum for BFO matrix and the α-Fe_2O_3 phase.

	Bi	Fe	O
BFO	24%	18%	58%
α-Fe_2O_3	2%	32%	66%

with the electron beam parallel to the [001] direction (*c* direction) of pseudo-cubic BFO. As for the results from the cross-sectional EDPs of Figures 1b and 1c, the strong spots denoted by a square are reflections from the BFO phase, and several sets of extra weak spots are reflections from the parasitic phase. When only one particle

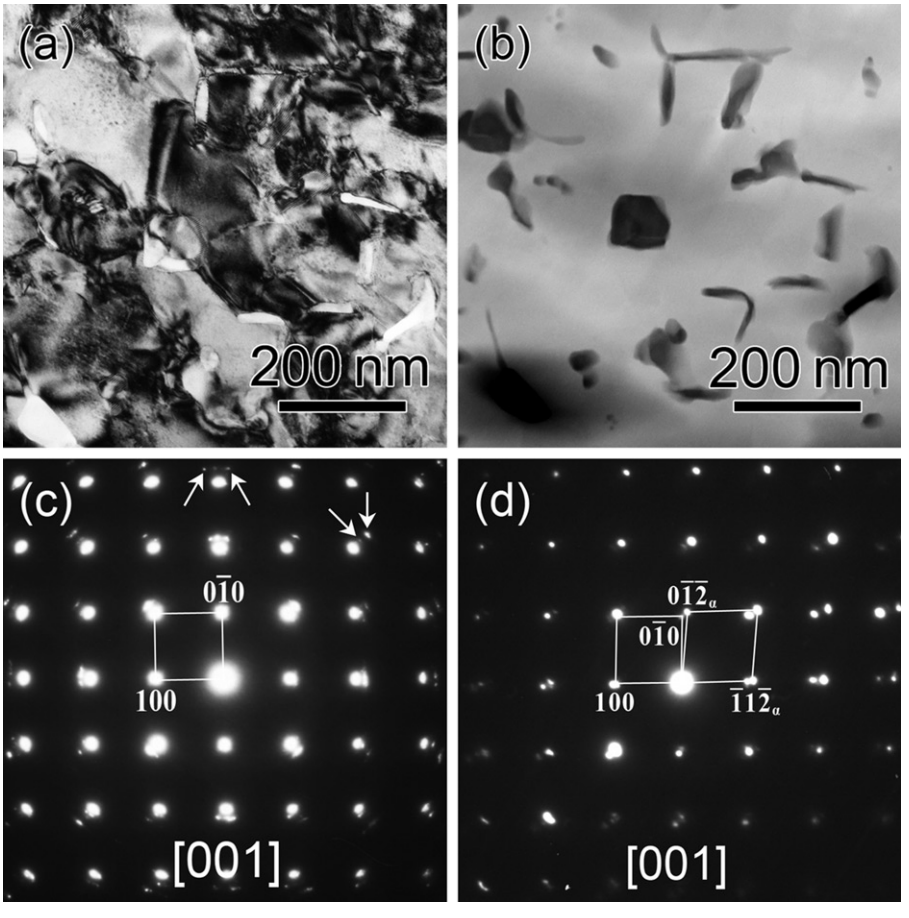

Figure 3. (a) Plan-view bright-field image showing the distributions of α-Fe_2O_3 particles in the Bi–Fe–O films grown at the oxygen pressure of 1 Pa. (b) HAADF image corresponding to (a). (c) Plan-view selected area electron diffraction pattern taken from the area covering both BFO and numerous α-Fe_2O_3 particles. (d) Plan-view selected area electron diffraction pattern taken from the area covering the BFO matrix and one α-Fe_2O_3 particle only.

of the parasitic phase and BFO matrix is included, the corresponding selected-area EDP displays one whole set of diffraction spots from one particle, as shown in Figure 3d. Detailed analysis of Figure 3c can be found in the following.

In combination with the results of EDS composition analysis and EDPs of three zone axes, we can deduce that the parasitic phase in the BFO films grown at 1 Pa oxygen pressure is rhombohedral α-Fe_2O_3. The calculated spacing distances of different low-index planes of secondary phase from EDPs given in Table 2 also support the identification. In Table 2, considering the measure accuracy from electron diffraction pattern, the measured inter-planar spacings and angles between the principal planes normal based on EDPs of Figures 1b, 1c and 3d are in good agreement with the calculated values of α-Fe_2O_3 (hematite) based on the published data in JCPDS.

Table 2. Comparison of d spacings and θ of α-Fe_2O_3 measured from EDPs with the calculated values based on JCPDS. θ is the angle between two indexed planes.

Fig.	Parameter	Measured values based on EDPs	Calculated values based on JCPDS	Zone axis of α-Fe_2O_3	Zone axis of BFO	Geometric relationships of the two zone axes based on EDPs	Deviation angle of the two zone axes based on the proposed OR
1b	$d_{\bar{1}1\bar{2}}$	3.72 Å	3.684 Å	[241]	[010]	deviated by a few degrees	2.98°
	$d_{\bar{1}02}$	3.72 Å	3.684 Å				
	θ	84.9°	86.0°				
1c	$d_{\bar{1}0\bar{4}}$	2.71 Å	2.700 Å	[010]	[$\bar{1}$10]	parallel	0°
	$d_{\bar{1}02}$	3.74 Å	3.684 Å				
	θ	83.9°	84.1°				
3d	$d_{\bar{1}1\bar{2}}$	3.74 Å	3.684 Å	[$\bar{4}\bar{2}$1]	[001]	deviated by a few degrees	2.98°
	$d_{0\bar{1}\bar{2}}$	3.71 Å	3.684 Å				
	θ	84.8°	86.0°				

The orientation relationships (ORs) between α-Fe_2O_3 and BFO film can be established from the superposed EDP in Figure 1c. The orientation relationships between rhombohedral α-Fe_2O_3 and pseudo-cubic BFO are determined to be

$$\text{OR}: (001)_{\alpha\text{-}Fe_2O_3}//(111)_{\text{p-BFO}}, \text{ and } [010]_{\alpha\text{-}Fe_2O_3}//[\bar{1}10]_{\text{p-BFO}}.$$

This OR is different from the one proposed by Lim et al., which is $[102]_{\alpha\text{-}Fe_2O_3}//[100]_{\text{p-BFO}}$, and $[1\bar{1}2]_{\alpha\text{-}Fe_2O_3}//[010]_{\text{p-BFO}}$ [27], but agrees well with other rhombohedral/cubic system like α-Fe_2O_3/γ-Fe_2O_3 [29] and α-Al_2O_3/Nb [30] system. Further investigation of EDPs in Figures 1b, 3c and 3d confirms this conclusion. In order to better see the relationships, a stereographic projection is drawn to visualize this OR, as shown in Figure 4a. Based on Figure 1c, if we set $[010]_{\alpha\text{-}Fe_2O_3}$ parallel to $[\bar{1}10]_{\text{p-BFO}}$, and $(001)_{\alpha\text{-}Fe_2O_3}$ parallel to $(111)_{\text{p-BFO}}$ in the stereographic projection, then some other parallel relationships can easily be established: $[001]_{\alpha\text{-}Fe_2O_3}//[111]_{\text{p-BFO}}$, $[\bar{1}00]_{\alpha\text{-}Fe_2O_3}//[\bar{1}01]_{\text{p-BFO}}$, and $[\bar{1}\bar{1}0]_{\alpha\text{-}Fe_2O_3}//[0\bar{1}1]_{\text{p-BFO}}$. From Figure 4a, it is suggested that the [241] and [$\bar{4}\bar{2}$1] directions of α-Fe_2O_3 deviate by 2.98° from the [010] and [001] directions of pseudo-cubic BFO, respectively. This is in agreement with the fact that the zone axes of BFO and α-Fe_2O_3 are not exactly parallel, as demonstrated in Figures 1b and 3d. The geometric relationships between the zone axes of BFO and α-Fe_2O_3 based on experiment EDPs and proposed ORs are summarized in Table 2.

The superposed EDPs of Figure 3c can be explained from the viewpoint of crystallographic symmetry of pseudo-cubic BFO. In addition to the ORs discussed above, due to four equivalent {111} planes of pseudo-cubic BFO, three different settings of the ORs are established as

$$\text{Variant 2}: (001)_{\alpha\text{-}Fe_2O_3}//(\bar{1}11)_{\text{p-BFO}}, \text{ and } [010]_{\alpha\text{-}Fe_2O_3}//[\bar{1}\bar{1}0]_{\text{p-BFO}},$$

$$\text{Variant 3}: (001)_{\alpha\text{-}Fe_2O_3}//(\bar{1}\bar{1}1)_{\text{p-BFO}}, \text{ and } [010]_{\alpha\text{-}Fe_2O_3}//[1\bar{1}0]_{\text{p-BFO}},$$

$$\text{Variant 4}: (001)_{\alpha\text{-}Fe_2O_3}//(1\bar{1}1)_{\text{p-BFO}}, \text{ and } [010]_{\alpha\text{-}Fe_2O_3}//[110]_{\text{p-BFO}}.$$

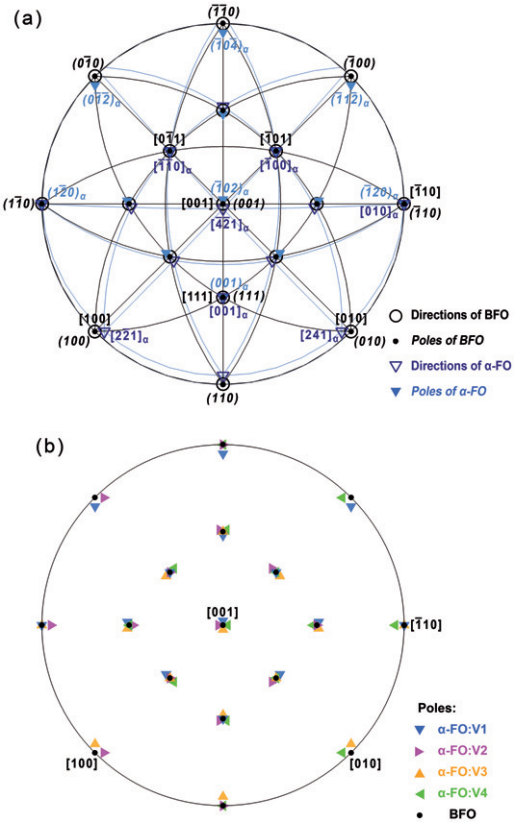

Figure 4. A stereographic projection showing the orientation relationships between α-Fe_2O_3 phase and BFO: (a) variant 1 only; (b) variants 1–4 included.

All four settings of the ORs are drawn in the stereographic projection shown in Figure 4b. In order to highlight all poles in the stereographic projection, we have ignored the projections of some directions, such as $[0\bar{1}1]$ and $[\bar{1}01]$, etc., as shown in Figure 4a. In Figure 3c, the splitting of the extra spots around [100] and [010] of BFO denoted by two arrows may result from all four variants as the multiple spots depicted in Figure 4b. Extra spots around [110] and $[\bar{1}10]$ of BFO denoted by arrows correspond to the superposed $(\bar{1}20)$ and $(\bar{1}0\bar{4})$ poles of four different variants of α-Fe_2O_3 particles, as demonstrated in Figure 4b. The split of these spots in Figure 3c is the result of superposed $(\bar{1}20)$ and $(\bar{1}0\bar{4})$ diffractions of four variants of α-Fe_2O_3 with different inter-planar spacings of 2.52 Å and 2.70 Å, respectively. Other extra spots can be analyzed in a similar way. The results from the stereographic projection match well with the experimental EDPs, which clarifies the ORs rationality.

Lattice mismatch and the strain relaxation mechanism play an important role in thin film growth. In order to investigate precipitate–matrix interfaces at an atomic scale, high-resolution transmission electron microscopy (HRTEM) was carried out. Figure 5a shows a cross-sectional lattice image taken along [010] of BFO showing the

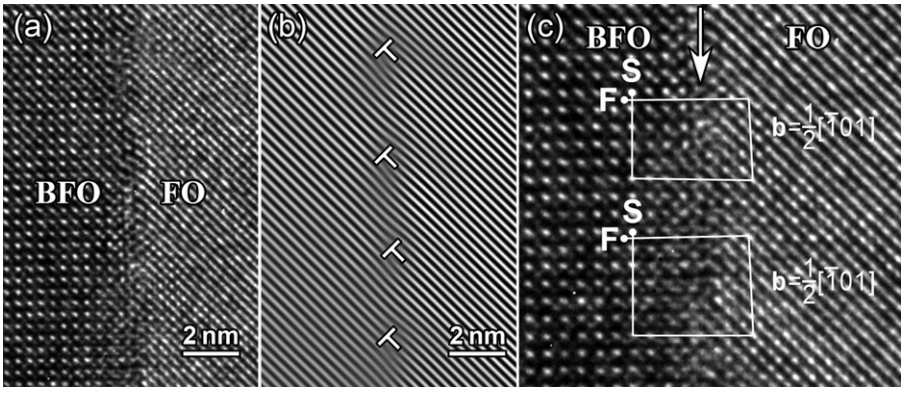

Figure 5. (a) Cross-sectional lattice image of α-Fe_2O_3/BFO interface area taken along [010] of BFO. (b) Fourier-filtered image of (a) gives prominence to the configuration of the dislocations. (c) Enlarged pattern of (a) showing the interfacial dislocations with Burgers vector $\frac{1}{2}[\bar{1}01]$.

boundaries between BFO and α-Fe_2O_3. Figure 5b shows the corresponding Fourier-filtered image by keeping only one of the Fourier components. It can be noticed that nearly periodic dislocations appear at the interfaces between the BFO film and α-Fe_2O_3 phase. The configurations of these misfit dislocations indicate that α-Fe_2O_3 particles are semi-coherently embedded in the film. Figure 5c shows an enlarged pattern of Figure 5a showing details at the interface. The dislocations are present at the interface and two Burgers circuits are drawn around the dislocations. From the HRTEM images we can only determine the Burgers vector component perpendicular to the direction of the incident electron beam. The component of Burgers vector **b** is determined to be $\frac{1}{2}[\bar{1}01]$. Usually, the dislocations in perovskite compounds have Burgers vectors of $\langle 100\rangle$ or $\langle 110\rangle$, and the dislocations in sapphire structure have Burgers vectors of $\frac{1}{3}\langle 11\bar{2}0\rangle$, which correspond to $[\bar{1}10]$, $[\bar{1}01]$, and $[0\bar{1}1]$ of pseudo-cubic BFO in proposed OR, respectively. As a result, it is more likely that the Burgers vectors of these misfit dislocations are $\frac{1}{2}[\bar{1}01]$.

The mismatch between the film and the substrate was considered. In general, providing that SRO layers are fully strained and have the same lattice parameter as STO, epitaxial $(001)_p$ BFO films are subjected to a compressive strain due to the lattice mismatch of -1.4%. Our X-ray diffraction θ–2θ scans results show (not shown here) that the out-of-plane lattice parameter of both films is 3.968 Å, which is quite close to bulk value of BFO (3.962 Å) [17]. This indicates that the film/substrate misfit strain is fully relaxed in this film system. Typically, the misfit strain between the film and the substrate is relaxed by the generation of misfit dislocations at the interface. However, in our experiment, both low magnification diffraction-contrast BF image and high-resolution lattice image show less misfit dislocations over a long distance at the interface area between the BFO films and the SRO/STO substrates, which indicates that another strain relaxation mechanism rather than the formation of misfit dislocations is dominant in this two phase film system. It is possible that the existence of α-Fe_2O_3 in the present BFO film changes the relaxation behavior of the

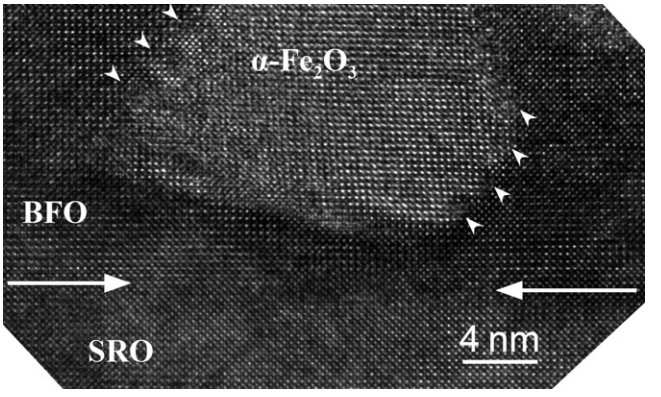

Figure 6. Cross-sectional HRTEM image taken along [010] of BFO film grown at 1 Pa showing one α-Fe_2O_3 particle originating from the film/substrate interface.

misfit strain between the film and the substrate. Figure 6 shows a HRTEM image showing one α-Fe_2O_3 particle lying at the BFO/SRO interface viewed along $[010]_{p\text{-}BFO}$. It seems that the α-Fe_2O_3 particle nucleates at a BFO/SRO interfacial step. The dislocations denoted by white arrows at the α-Fe_2O_3/BFO interface have Burgers vectors $\frac{1}{2}\langle 101\rangle$. Due to the fact that the inter-planar spacing of $(1\bar{1}2)_{\alpha\text{-}Fe_2O_3}$ is 3.68 Å, which is much smaller than that of $(100)_p$ of BFO (3.96 Å), it is proposed that the formation of the α-Fe_2O_3 phase should release the elastic misfit strain between the film and the substrate.

3.2. *Bi–Fe–O film grown under oxygen pressure of 0.3 Pa*

For comparison, the BFO film grown at an oxygen pressure of 0.3 Pa was investigated by the same TEM methods as used for the film grown at 1 Pa. The results show that α-Fe_2O_3 particles also exist and have the same ORs as in the film grown at 1 Pa. The distributions of α-Fe_2O_3 phase in both films deposited at oxygen pressures of 1 Pa and 0.3 Pa were investigated and are compared in Figure 7. In low-magnification Z-contrast cross-sectional and plan view images, the contours of α-Fe_2O_3 particles are clearly seen. Films grown at 1 Pa and 0.3 Pa oxygen pressure show similar morphologies; the interfaces between BFO and α-Fe_2O_3 are typically parallel to $\{01\bar{1}2\}$ planes of the hexagonal unit cell ($\{012\}$ planes of morphological unit cell of α-Fe_2O_3). It is worth noting that both the density and sizes of α-Fe_2O_3 particles increase and the regularity is relatively low when the deposition pressure is reduced, as seen in Figures 7c and 7d.

Moreover, in addition to α-Fe_2O_3, another parasitic phase was observed near the interface between the BFO film grown at 0.3 Pa oxygen pressure and the SRO layer. Figure 8a shows a cross-sectional bright field image of the 0.3 Pa sample showing the BFO/SRO interface region. Besides large vertical α-Fe_2O_3 particles with a width of more than 40 nm, some small precipitates with Moiré fringe contrast can be identified in the first 30 nm area of the BFO film. Their size is about 10 nm in width.

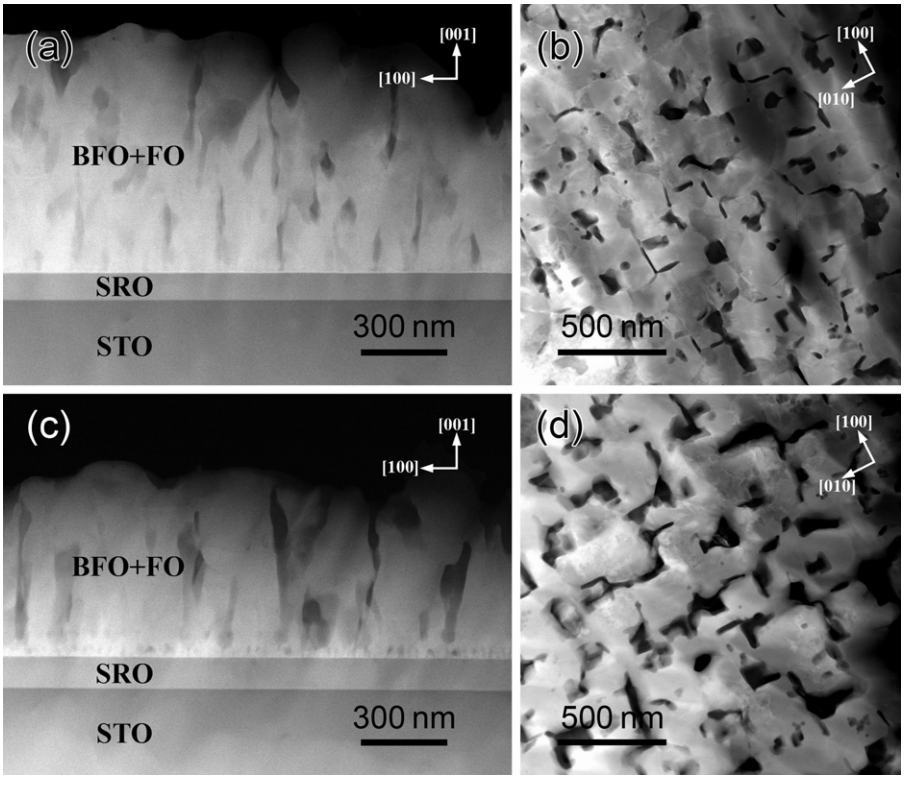

Figure 7. Low-magnification HAADF image showing different dimensions of the parasitic phases in the films grown at different oxygen pressures. (a) Cross-sectional image and (b) plan-view image of the film grown at 1 Pa. (c) Cross-sectional image and (d) plan-view image of the film grown at 0.3 Pa.

The corresponding HAADF image in Figure 8b indicates that theses precipitates are poor in heavy elements. Figure 8c shows a selected area EDP taken from the area covering both these small precipitates and the BFO matrix. The left white square symbolizes the unit cell of BFO. Besides the strong diffractions from BFO, weak diffraction spots from the precipitates are observed and indexed as Fe_3O_4. Its unit cell is outlined by the right white square. The magnetite phase Fe_3O_4 has a spinel structure with the lattice parameter of 8.386 Å (JCPDS No. 19-0629). It should be pointed out that γ-Fe_2O_3 shares a similar structure and lattice parameters with cubic Fe_3O_4, which makes it difficult to distinguish them by TEM. However, their space groups are different: $P4_132$ for γ-Fe_2O_3 (JCPDS No. 39-1346) and $Fd\text{-}3m$ for Fe_3O_4 (JCPDS No. 19-0629), which may facilitate the determination of these two phases. Based on the different forbidden reflections, {110} reflections are forbidden in Fe_3O_4 whereas they are present in γ-Fe_2O_3. The precipitates were indexed as Fe_3O_4 rather than γ-Fe_2O_3 since we did not observe {110} reflections in Figure 8c; but we cannot completely exclude the existence of γ-Fe_2O_3 as the intensities of {110} reflections are relatively weak. In addition, the orientation relationships between Fe_3O_4 precipitates and the

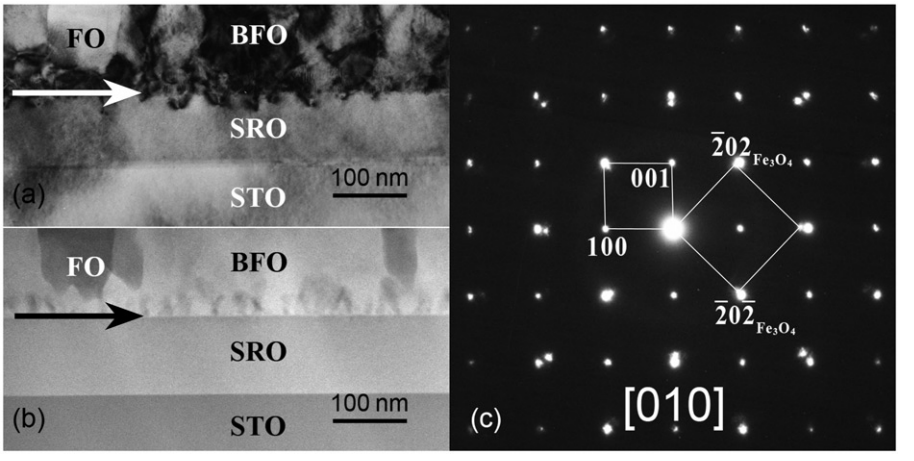

Figure 8. (a) Low-magnification cross-sectional bright-field image of the films prepared at 0.3 Pa oxygen pressure showing the Fe_3O_4 phase precipitates near the film/substrate interface. Interfacial dislocations can be found 10–20 nm away from the interface. (b) HAADF image of the same area as in (a). (c) Cross-sectional selected area diffraction pattern taken from the area covering both the Fe_3O_4 precipitates and BFO film matrix.

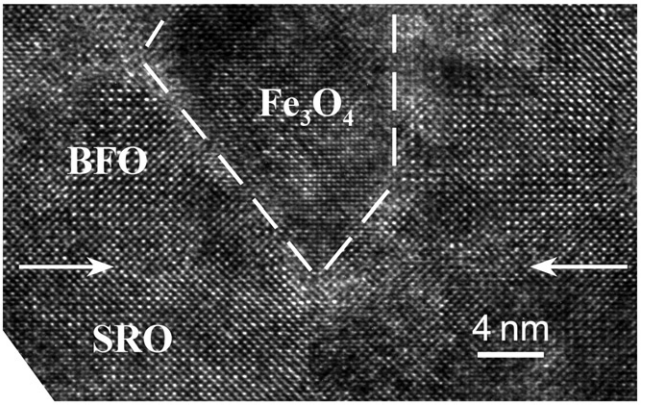

Figure 9. Cross-sectional HRTEM image viewed along [010] direction of the BFO film grown at 0.3 Pa showing Fe_3O_4 precipitate lying on the plane of films.

BFO matrix are determined to be $(001)_{Fe_3O_4}//(001)_{p\text{-}BFO}$, and $[010]_{Fe_3O_4}//[010]_{p\text{-}BFO}$. This is in agreement with epitaxial $BiFeO_3$–$NiFe_2O_4$ film systems, in which $NiFe_2O_4$ also has a spinel structure [31].

Figure 9 displays a cross-sectional HRTEM image showing one Fe_3O_4 precipitate lying on the planes of films viewed along the [010] direction of BFO. It seems that the Fe_3O_4 precipitate originates from the BFO/SRO interface. The fact that the dislocations are observed around the boundary between the secondary phase and the

BFO matrix indicates that the Fe_3O_4 precipitate is also semi-coherent embedded in the BFO film matrix. Because the inter-planar spacing of (400) of Fe_3O_4 (2.10 Å) is larger than that of $(200)_p$ of BFO (1.98 Å), the formation of these Fe_3O_4 precipitates near the BFO/SRO interface may increase the compressive film/substrate mismatch strain. The increased compressive strain induces the formation of interfacial dislocations at the interfacial area, as seen in Figure 8a. These dislocations lie 10–20 nm away from the interface at SRO side and distribute approximately periodically with the distance of around 45 nm. Unlike the film grown under pressure of 1 Pa, in which the misfit strain is fully relaxed by the formation of the semi-coherent α-Fe_2O_3 phase, when the deposition pressure is reduced to 0.3 Pa, the misfit strain at the film/substrate interface is increased by the formation of Fe_3O_4 precipitates. As a result, the interfacial dislocations as well as the secondary phase form to relax the compressive elastic misfit strain in this system.

3.3. *The oxidation states of Fe in the films*

The oxidation states of Fe are of importance to understand the electronic structures of the films. In order to identify the oxidation states of Fe, XPS spectra were collected for Fe 2*p* with different periods of ion bombardment on the surface of the sample prepared at 1 Pa of oxygen. The velocity of ion bombardment was 0.2 nm/s. As a result, approximately 12 nm, 24 nm, 48 nm and 72 nm of the films were removed from the surface following the bombardment for 60 s, 120 s, 240 s and 360 s, respectively. The results are shown in Figure 10. It is easy to realize that the iron at the surface is present in the Fe^{3+} oxidized state, which is confirmed by the characteristic satellite structure at approximately 8 eV above from the position of Fe $2p_{3/2}$ peak at 711 eV [32,33]. The vertical line denotes the positions of the

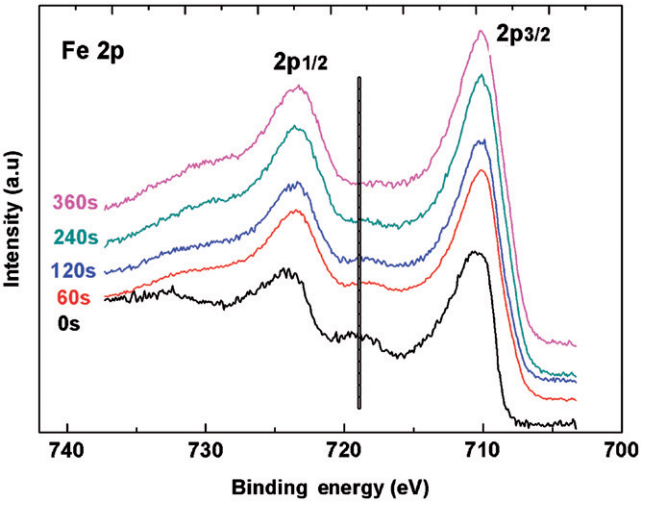

Figure 10. The in-depth profile of X-ray photoelectron spectra of Fe 2*p* lines showing the oxidized Fe^{3+} form in the film grown at 1 Pa pressure.

satellite peaks. After Ar^+ etching, the intensity of the satellite peaks gradually decreases until it disappears due to Fe^{3+} to Fe^{2+} reduction induced by Ar^+ bombardment, which is a well-documented process reported previously in the literature [34,35]. Since the iron valence is 3+ in α-Fe_2O_3 and in $BiFeO_3$ [36], the XPS results show that the films contain Fe in the +3 valence state, which may come from both the $BiFeO_3$ matrix and α-Fe_2O_3 secondary phase, consistent with the TEM results.

3.4. *Discussion*

As reported previously [9,13], single phase BFO films grown by pulsed laser deposition are obtained in the range 1–2.6 Pa of oxygen. In the present work, a mixture of BFO and α-Fe_2O_3 phase was obtained. It is worth pointing out that besides oxygen pressure other factors including substrate temperature, target nominal composition, and deposition method are different from the previous reports. It is usually believed that the formation of iron oxide precipitates is due to several factors such as deficiency of Bi content in the target, low oxygen pressure, and high substrate temperature, etc., in which Bi deficiency plays a much important role. The deposition conditions in the present study were deviated from known optimal conditions. On the one hand, the target compositions were much different. 5% excess Bi was adopted to prepare the present films compared with 15% excess Bi in Bea et al.'s films [9]. On the other hand, substrate temperature was kept at 550°C, which was lower than those, usually 580°C or 600°C, for optimized films [9,13]. The formation of α-Fe_2O_3 phase may mainly be the result of Bi deficiency due to its high volatility. When other growth conditions are the same, the level of oxygen pressure during the deposition becomes vital due to the high vapor pressure of Bi. If the oxygen pressure is low, the evaporation becomes strong and the deposition rate is relatively slow. It was reported that the growth of the particles is controlled by surface diffusion process and thus the lateral size of the particles increases as the growth rate decreases [24]. In our films, it is reasonable that the sizes of the α-Fe_2O_3 phase increase when the deposition pressure is decreased. Moreover, due to the fact that Bi is more unstable than Fe, the film grown under low deposition pressure contains less Bi. As a result, the amount of α-Fe_2O_3 slightly increased. It is well known that the α-Fe_2O_3 phase is an antiferromagnetic phase. Its existence reduces the leakage current and improves the ferroelectric properties of the films [11]. Since the leakage current was reduced when the oxygen vacancies decreased by post-annealing in BFO films [21,37], one explanation of the lower leakage current is the transportation of oxygen from the secondary phase to BFO. Our EDS composition quantification result shows that oxygen concentration is slightly higher in the α-Fe_2O_3 phase than in the BFO film matrix, which indicates that the presence of the α-Fe_2O_3 phase may be the source of oxygen and may reduce the oxygen vacancies in BFO films.

The existence of the Fe_3O_4 phase in the as-grown Bi–Fe–O films has not been reported much previously. In this work, a nano-sized Fe_3O_4 phase forms in the 0.3 Pa film and accumulates in the area near the BFO/SRO interface. Because the valences of iron in these Fe_3O_4 precipitates are a mixture of +3 and +2, the formation of them

may ascribe to the oxygen deficiency near the interfacial area in low oxygen conditions. The ferrimagnetic arrangements of Fe^{3+} and Fe^{2+} in the Fe_3O_4 phase may cause a large magnetization of the film.

4. Conclusions

Conventional TEM analysis combined with HAADF imaging and EDS composition plots revealed that Bi–Fe–O films prepared at oxygen pressures of 1 Pa and 0.3 Pa consist of both BFO and antiferromagnetic α-Fe_2O_3 phases. By decreasing oxygen pressure, the density and the size of α-Fe_2O_3 phase increase. The ferromagnetic phase Fe_3O_4 only exists in the films prepared under 0.3 Pa oxygen pressure. Both α-Fe_2O_3 particles and Fe_3O_4 precipitates are semi-coherently embedded in the BFO matrix. High-resolution transmission electron microscopy observations on a large view area show that less misfit dislocations can be identified along the interfaces between the BFO films and the SRO/STO substrates indicating that the formation of secondary phase may be a major contributor to the misfit relaxation in these heteroepitaxy systems. Using XPS it was clarified that Fe is in the 3+ oxidation states in both films.

Acknowledgements

This work was supported by the National Basic Research Program of China (2009CB623705), and the National Natural Science Foundation of China (No. 50871115 and No. 10874226). We would like to thank Ms. Bin Zhang for the help with XPS measurement.

References

[1] N.A. Spaldin and M. Fiebig, Science 309 (2005) p.391.
[2] W. Eerenstein, N.D. Mathur and J.F. Scott, Nature 442 (2006) p.759.
[3] N.A. Hill, J. Phys. Chem. B 104 (2000) p.6694.
[4] G. Catalan and J.F. Scott, Adv. Mater. 21 (2009) p.2463.
[5] J. Wang, J.B. Neaton, H. Zheng, V. Nagarajan, S.B. Ogale, B. Liu, D. Viehland, V. Vaithyanathan, D.G. Schlom, U.V. Waghmare, N.A. Spaldin, K.M. Rabe, M. Wuttig and R. Ramesh, Science 299 (2003) p.1719.
[6] D. Lebeugle, D. Colson, A. Forget, M. Viret, P. Bonville, J.F. Marucco and S. Fusil, Phys. Rev. B 76 (2007) p.024116.
[7] T. Zhao, A. Scholl, F. Zavaliche, K. Lee, M. Barry, A. Doran, M.P. Cruz, Y.H. Chu, C. Ederer, N.A. Spaldin, R.R. Das, D.M. Kim, S.H. Baek, C.B. Eom and R. Ramesh, Nat. Mater. 5 (2006) p.823.
[8] D. Lebeugle, D. Colson, A. Forget, M. Viret, A.M. Bataille and A. Gukasov, Phys. Rev. Lett. 100 (2008) p.227602.
[9] H. Bea, M. Bibes, A. Barthelemy, K. Bouzehouane, E. Jacquet, A. Khodan, J.P. Contour, S. Fusil, F. Wyczisk, A. Forget, D. Lebeugle, D. Colson and M. Viret, Appl. Phys. Lett. 87 (2005) p.072508.
[10] H. Bea, M. Bibes, S. Fusil, K. Bouzehouane, E. Jacquet, K. Rode, P. Bencok and A. Barthelemy, Phys. Rev. B 74 (2006) p.020101.
[11] S. Fujino, M. Murakami, S.H. Lim, M. Wuttig, L.G. Salamanca-Riba and I. Takeuchi, Solid State Ionics 178 (2007) p.1257.

[12] W. Eerenstein, F.D. Morrison, J. Dho, M.G. Blamire, J.F. Scott and N.D. Mathur, Science 307 (2005) p.1203a.
[13] M. Murakami, S. Fujino, S.H. Lim, L.G. Salamanca-Riba, M. Wuttig, I. Takeuchi, B. Varughese, H. Sugaya, T. Hasegawa and S.E. Lofland, Appl. Phys. Lett. 88 (2006) p.112505.
[14] J. Wang, A. Scholl, H. Zheng, S.B. Ogale, D. Viehland, D.G. Schlom, N.A. Spaldin, K.M. Rabe, M. Wuttig, L. Mohaddes, J. Neaton, U. Waghmare, T. Zhao and R. Ramesh, Science 307 (2005) p.1203b.
[15] W.B. Luo, J. Zhu, Y.R. Li, X.P. Wang, D. Zhao, J. Xiong and Y. Zhang, Appl. Phys. Lett. 91 (2007) p.082501.
[16] X.J. Lou, C.X. Yang, T.A. Tang, Y.Y. Lin, M. Zhang and J.F. Scott, Appl. Phys. Lett. 90 (2007) p.262908.
[17] D.H. Kim, H.N. Lee, M.D. Biegalski and H.M. Christen, Appl. Phys. Lett. 92 (2008) p.012911.
[18] H.W. Jang, S.H. Baek, D. Ortiz, C.M. Folkman, R.R. Das, Y.H. Chu, P. Shafer, J.X. Zhang, S. Choudhury, V. Vaithyanathan, Y.B. Chen, D.A. Felker, M.D. Biegalski, M.S. Rzchowski, X.Q. Pan, D.G. Schlom, L.Q. Chen, R. Ramesh and C.B. Eom, Phys. Rev. Lett. 101 (2008) p.107602.
[19] R.R. Das, D.M. Kim, S.H. Baek, C.B. Eom, F. Zavaliche, S.Y. Yang, R. Ramesh, Y.B. Chen, X.Q. Pan, X. Ke, M.S. Rzchowski and S.K. Streiffer, Appl. Phys. Lett. 88 (2006) p.242904.
[20] L. You, N.T. Chua, K. Yao, L. Chen and J.L. Wang, Phys. Rev. B 80 (2009) p.024105.
[21] H. Yang, Y.Q. Wang, H. Wang and Q.X. Jia, Appl. Phys. Lett. 96 (2010) p.012909.
[22] G.W. Pabst, L.W. Martin, Y.H. Chu and R. Ramesh, Appl. Phys. Lett. 90 (2007) p.072902.
[23] H. Zheng, J. Wang, S.E. Lofland, Z. Ma, L. Mohaddes-Ardabili, T. Zhao, L. Salamanca-Riba, S.R. Shinde, S.B. Ogale, F. Bai, D. Viehland, Y. Jia, D.G. Schlom, M. Wuttig, A. Roytburd and R. Ramesh, Science 303 (2004) p.661.
[24] H.M. Zheng, F. Straub, Q. Zhan, P.L. Yang, W.K. Hsieh, F. Zavaliche, Y.H. Chu, U. Dahmen and R. Ramesh, Adv. Mater. 18 (2006) p.2747.
[25] J.L. MaCmanus-Driscoll, P. Zerrer, H.Y. Wang, H. Yang, J. Yoon, A. Fouchet, R. Yu, M.G. Blamire and Q.X. Jia, Nat. Mater. 7 (2008) p.314.
[26] H. Yang, H.Y. Wang, J. Yoon, Y.Q. Wang, M. Jain, D.M. Feldmann, P.C. Dowden, J.L. MacManus-Driscoll and Q.X. Jia, Adv. Mater. 21 (2009) p.3794.
[27] S.H. Lim, M. Murakami, W.L. Sarney, S.Q. Ren, A. Varatharajan, V. Nagarajan, S. Fujino, M. Wuttig, I. Takeuchi and L.G. Salamanca-Riba, Adv. Funct. Mater. 17 (2007) p.2594.
[28] F. Kubel and H. Schmid, Acta Crystallogr. B: Struct. Sci. 46 (1990) p.698.
[29] S. Kachi, S. Shimizu and K. Momiyama, J. Phys. Soc. Jpn. 18 (1963) p.106.
[30] J. Mayer, C.P. Flynn and M. Ruhle, Ultramicroscopy 33 (1990) p.51.
[31] Q. Zhan, R. Yu, S.P. Crane, H. Zheng, C. Kisielowski and R. Ramesh, Appl. Phys. Lett. 89 (2006) p.172902.
[32] D. Kothari, V.R. Reddy, A. Gupta, D.M. Phase, N. Lakshmi, S.K. Deshpande and A.M. Awasthi, J. Phys. Condens. Matter 19 (2007) p.136202.
[33] M. Popa, S. Preda, V. Fruth, K. Sedlackova, C. Balazsi, D. Crespo and J.M. Calderon-Moreno, Thin Solid Film 517 (2009) p.2581.
[34] E. Paparazzo, J.L. Dormann and D. Fiorani, Phys. Rev. B 28 (1983) p.1154.
[35] N.S. McIntyre and D.G. Zetaruk, Anal. Chem. 49 (1977) p.1521.
[36] O. Gautreau, C. Harnagea, L. Gunawan, G.A. Botton, F. Normandin, T. Veres, L. Pintilie, M. Alexe and A. Pignolet, J. Phys. D Appl. Phys. 41 (2008) p.112002.
[37] C. Wang, M. Takahashi, H. Fujino, X. Zhao, E. Kume, T. Horiuchi and S. Sakai, J. Appl. Phys. 99 (2006) p.054104.